e-Journal of Nondestructive Testing - ISSN 1435-4934 - www.ndt.net

14th Conference on Industrial Computed Tomography, Antwerp, Belgium (iCT 2025), www.ict2025.org

Single X-ray Projection Material Decomposition using a Mesh Projector

Fleur Linsen[1], Domenico Iuso[1,2], Jan Sijbers[1,2]

[1]imec-Vision Lab, Department of Physics, University of Antwerp, Antwerp, Belgium

[2]DynXlab: Center for 4D Quantitative X-ray Imaging and Analysis, Antwerp, Belgium

Abstract

This study presents a method for estimating the mass fractions of chemical elements in an object, which is modeled as a homogeneous mixture, using a single X-ray radiograph and its surface mesh. The method assumes that the chemical elements in the mixture and their mass attenuation coefficients are known. A stochastic gradient descent algorithm is used to iteratively minimize the error between a scanned radiograph and a simulated polychromatic radiograph, enabling the estimation of mass fractions. The CAD-ASTRA toolbox is employed to compute the path-lengths and simulate polychromatic X-ray radiographs for test objects under varying noise conditions [1].

1 Introduction

X-ray imaging is a well-known technique for non-destructive imaging and characterization of objects. Based on X-ray radiography, information can be gained of an object's shape, density and atomic number. These features make X-ray imaging highly suitable for non-destructive analysis and testing. A key technique in non-destructive radiography-based analysis is material decomposition, whose aim is to determine the materials composition of an object. In medical imaging, material decomposition can be applied to distinguish between benign and malignant tumors [2]. In cargo inspection, material decomposition can be employed to recognize smuggling goods or impurities in agricultural products [3]. Two main techniques for material decomposition have been described in the literature: *Dual Energy Material Decomposition* (DEMD) and *Single Energy Material Decomposition* (SEMD).

DEMD exploits the energy dependency of the attenuation coefficients of materials. The linear attenuation coefficient as a function of the energy can be modeled as a linear combination of basis functions, such as those describing the energy dependency of the photoelectric interaction and total cross-section of the Compton scattering. Another approach is to choose the energy dependent attenuation of basis materials, such as bone and water, as basis functions [4].[5]. This technique enables to reveal differences in attenuation which are invisible in conventional reconstructions. Another approach is acquiring high and low energy radiographs of an object, resulting in radiographs with distinct projection values [6]. Look-up tables are then used to link projection values to path lengths. Based on this information, the material thicknesses can be obtained. Reducing exposure requires an adaptation of the hardware, as for example dual-source units, or photon-counting detectors [4]. Furthermore, since DEMD requires two scans, radiation exposure to the object may be a concern, especially in medical imaging [4]. In addition, the creation of look-up tables may be time consuming [6] or inaccurate [7].

Single-energy projections (SEMD) on the other hand estimates the material composition from only one scan, by employing knowledge on the path-lengths. These path-lengths can either be estimated from a CT reconstruction [6] or from a surface image of the object obtained from a 3D laser scanner [8].

Recently, it was shown that path-lengths can also be directly recovered from few X-ray projections by registering surface meshes of objects to their scanned projections [9]. This method, which does not require additional hardware beyond the X-ray scanner or a full CT scan, offers potential for integration into material decomposition processes. Our proposed method estimates the chemical mass fractions of a homogeneous mixture of an object scanned with X-ray light. The CAD-ASTRA toolbox is applied for computing path-lengths and simulating polychromatic X-ray radiographs.

2 Methodology

Our proposed material composition estimation method relies on a single radiograph only and exploits prior knowledge of the object's surface mesh,its density and the set of possible chemical elements composing the object. The material is modeled as a homogeneous mixture of these chemical elements, whose linear attenuation coefficients are publicly available [10, 11]. The method is initialized with random mass fractions $\{x_n\}$ of the chemical elements in the mixture. The mass fractions are then iteratively refined through an optimization process. Mass fractions are estimated by minimizing a cost function that compares a scanned X-ray projection $\boldsymbol{p}$ of the object with a simulated projection:

$$\{\hat{x}_1, \cdots, \hat{x}_N\} = \arg \min_{x_1,\cdots,x_N} \left\| \boldsymbol{p} - \mathrm{PolyProj}_{\mathbf{m}}(\{x_n\}) \right\|_2^2 \quad , \tag{1}$$

The simulated projection is generated using the CAD-ASTRA mesh projector [1] and a poly-chromatic model for the forward projection simulation. Let $\boldsymbol{l}$ denote the vector of path-lengths from the source to the centre of each detector element and $\boldsymbol{m}$ be the surface mesh of the object. Then, the simulated projection is computed using the polychromatic forward operator $\mathrm{PolyProj}_{\mathbf{m}}$ [9],

https://doi.org/10.58286/30756

defined as:

$$\text{PolyProj}_{\mathbf{m}}(\{x_n\}) = \sum_{k=1}^{K} w_k \exp\left(-\sum_{n=1}^{N} \rho x_n \frac{\mu_{n,k}}{\rho_n} \boldsymbol{l}\right) \quad , \tag{2}$$

with N the total number of chemical elements in the mixture and K the number of energy bins of the source X-ray spectrum. Furthermore, the energy-dependent factor w_k is based on the spectral characteristics of the X-ray source and the detector's sensitivity for the k^{th} energy bin. Finally, $\frac{\mu_{n,k}}{\rho_n}$ is the mass attenuation coefficient of the n^{th} chemical element at the k^{th} energy bin. To evaluate its stability, the method is tested for different signal-to-noise ratios (SNR) by adjusting the radiant intensity (photons / steradian) . For each photon intensity, 50 optimal fractions are determined, each time starting from newly generated images containing variations in noise.

3 Experiments

Simulation experiments were set up to test the proposed fractions estimator using two objects. The first object was a rod, with a height of 19 *mm* and diameter of 7 *mm*, made of an alloy of Fe and C at 98 % Fe and 2 % C. The other object was a water bottle with a height of 241 *mm* and a diameter of 144 *mm*, consisting of a solution of hydrogen H, oxygen O, and chlorine Cl. The ground truth mass fractions for H, O, and Cl are 8%, 55,7%, and 36,3%, respectively.

The fractions were estimated from a single, polychromatic projection polluted with Poisson noise and an inhomogeneous distribution of photons over the detector pixels, to account for the inhomogeneous photon distribution in a cone-beam projection. For both projections, the object-detector distance equals 500 *mm*, while the source-object distance for the rod was 30 *mm* and 5000 *mm* for the bottle. The detector pixels were binned for an equivalent of 3×3 *mm*. Experiments were run for various SNR by varying the radiant intensity in the range 10^7 to 10^{13} ph/sr.

4 Results and discussion

Fig.1 shows the projections of the rod for the outer left (10^7 ph/sr), middle (10^{10} ph/sr) and outer right (10^{13} ph/sr) data points for the radiant intensities. The median of the estimated mass fractions for each radiant intensity, together with their 2.5th ($P_{2.5}$) and 97.5th ($P_{97.5}$) percentile are plotted in Fig. 2a and Fig. 2b. These graphs indicate that the method is able to accurately predict the mass fraction for radiant intensities of 10^{10} ph/sr and higher. This is confirmed by the numerical values in Table 1, which also shows the inter quartile range (IQR). The values of the IQR, $P_{2.5}$ and $P_{97.5}$ demonstrate that the accuracy increases with increasing radiant intensity.

It can be observed that for the same radiant intensities, the projections of the hydrochloric acid bottle, shown in Fig. 3, are noisier than those of the steel rod (Fig. 1). To magnify the rod in the images of Fig. 1, the distance between the source and the rod was chosen to be significantly shorter than the distance between the source and the bottle, while the distance between the object and the detector and the size of the detector elements were kept the same. The number of photons detected per detector element is therefore higher for the images of the rod (Fig. 1) than for the images of the bottle (Fig. 3), resulting in a higher SNR for the images in Fig. 1 than for the images in Fig. 3. This difference in the SNR affects the results, as can be seen in the graphs in Fig. 4. For a radiant intensity of 10^7 ph/sr and 10^8 ph/sr, the stochastic gradient descent algorithm seems to be unable to find a proper minimum. At 10^9, the stochastic gradient descent algorithm does converge to a minimum, but the predicted values for the mass fractions significantly differ from the true mass fractions. As for the experiments with the steel rod, the higher the radiant intensity is, the more accurately the mass fractions are estimated, as (cfr. Table 2). Based on the results from Table 2, the method can accurately predict the mass fractions starting from 10^{12} ph/sr.

5 Conclusion

The proposed method is able to stably predict the mass fractions of two distinct homogeneous mixtures, namely steel and hydrochloric acid, for different SNR of the X-ray projections. The accuracy and precision of the predictions increases for higher SNR, reaching good performance when the imaging quality is well within the imaging quality used in regular X-ray scans for baggage control or quality assurance. The method stands out as a promising technique to derive the mass fractions of a homogeneous mixture of multiple elements, from a single polychromatic X-ray radiograph. It holds potential for future endeavours to infer the material composition starting from a larger shortlist of elements.

Acknowledgements
This study was financially supported by Fonds voor Wetenschappelijk Onderzoek (S003421N, G090020N, G094320N).

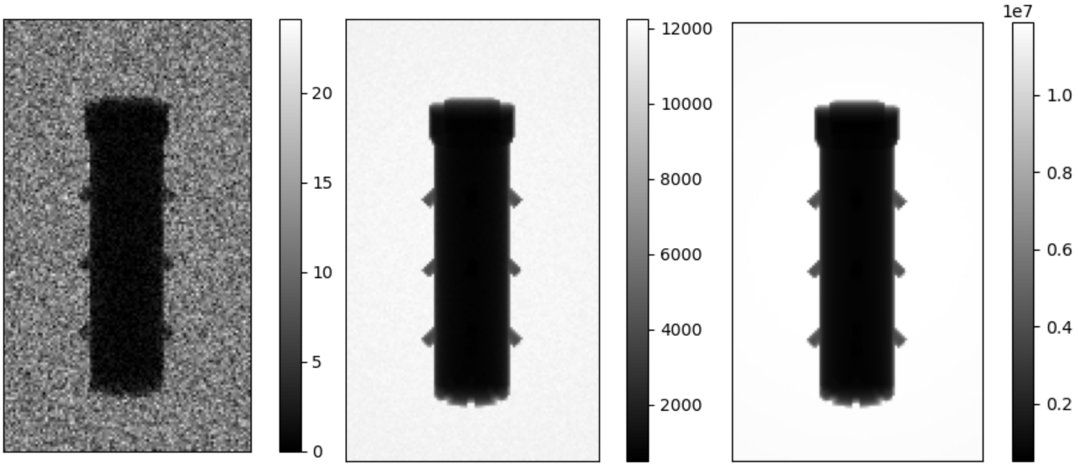

(a) 10^7 ph/sr (b) 10^{10} ph/sr (c) 10^{13} ph/sr

Figure 1: X-ray projections of the steel rod for a radiant intensity of 10^7 ph/sr (a), 10^{10} ph/sr (b) and 10^{13} ph/sr (c).

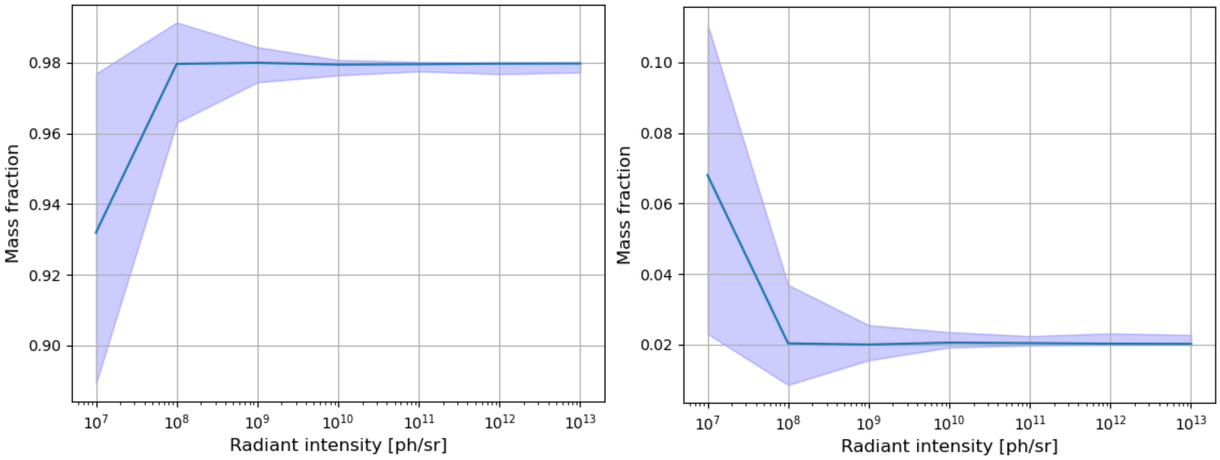

(a) Fe (b) C

Figure 2: Median mass fraction of Fe and C in function of the radiant intensity. The error band indicates the 2.5th and 97.5th percentile.

Rad. int. [ph/sr]	Median (IQR) (Fe)	$P_{2.5}$-$P_{97.5}$ (Fe)	Median (IQR) (C)	$P_{2.5}$-$P_{97.5}$ (C)
10^7	0.932 (0.037)	0.889-0.977	0.0681 (0.037)	0.023-0.111
10^8	0.980 (0.010)	0.963-0.991	0.020 (0.010)	0.009-0.037
10^9	0.980 (0.004)	0.974-0.984	0.020 (0.004)	0.016-0.026
10^{10}	0.979 (0.002)	0.976-0.981	0.021 (0.002)	0.019-0.024
10^{11}	0.980 (0.001)	0.977-0.980	0.020 (0.001)	0.020-0.022
10^{12}	0.980 (0.001)	0.977-0.980	0.020 (0.001)	0.020-0.023
10^{13}	0.980 (0.001)	0.977-0.980	0.020 (0.001)	0.020-0.023

Table 1: Mean and standard deviation (SD), median and 2.5th ($P_{2.5}$) and 97.5th ($P_{97.5}$) percentiles of the optimal fractions for Fe and C for different values of the radiant intensity (Rad.Int), expressed as the number of photons per steradian [ph/sr].

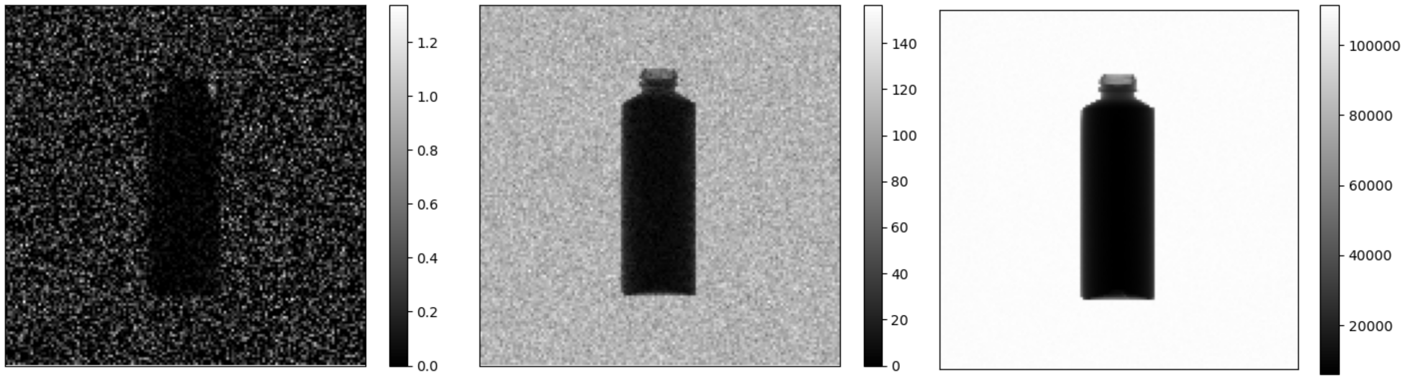

(a) 10^7 ph/sr (b) 10^{10} ph/sr (c) 10^{13} ph/sr

Figure 3: X-ray projections of the bottle of hydrochloric acid for a radiant intensity of 10^7 ph/sr (a), 10^{10} ph/sr (b) and 10^{13} ph/sr (c).

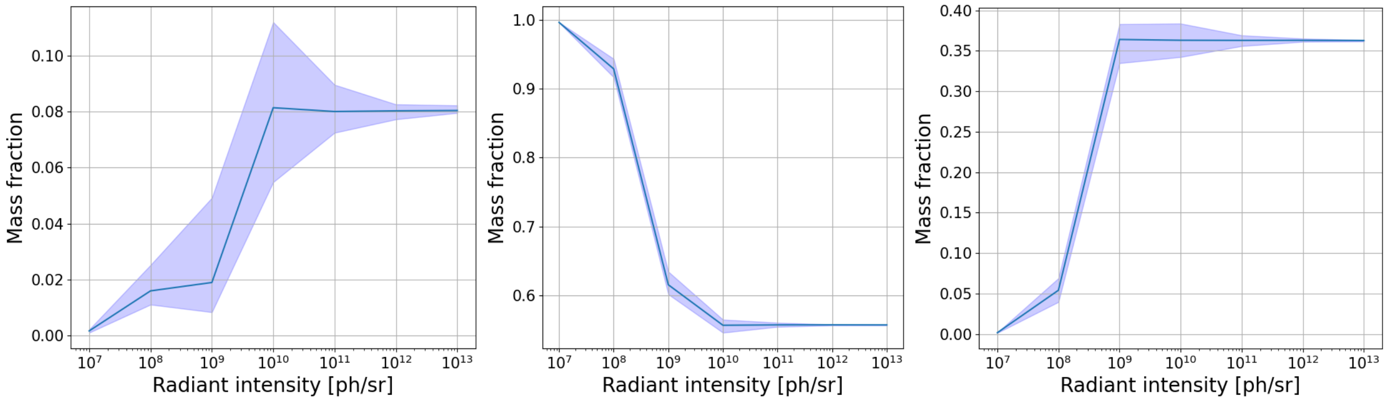

(a) H (b) O (c) Cl

Figure 4: Median mass fraction of H, O and Cl in function of the radiant intensity. The error band indicates the 2.5th and 97.5th percentile.

Rad. int. [ph/sr]	Median (IQR) (H)	$P_{2.5}$-$P_{97.5}$ (H)	Median (IQR) (O)	$P_{2.5}$-$P_{97.5}$ (O)	Median (IQR) (Cl)	$P_{2.5}$-$P_{97.5}$ (Cl)
10^7	0.002 (0.001)	0.001-0.002	0.991 (0.001)	0.996-0.997	0.002 (0.001)	0.001-0.002
10^8	0.016 (0.005)	0.011-0.025	0.929 (0.010)	0.917-0.944	0.054 (0.012)	0.040-0.069
10^9	0.019 (0.006)	0.008-0.049	0.615 (0.012)	0.601-0.634	0.364 (0.017)	0.335-0.383
10^{10}	0.081 (0.022)	0.055-0.112	0.556 (0.007)	0.545-0.564	0.363 (0.016)	0.342-0.384
10^{11}	0.080 (0.006)	0.072-0.081	0.557 (0.002)	0.554-0.560	0.363 (0.004)	0.356-0.369
10^{12}	0.080 (0.002)	0.077-0.083	0.557 (0.001)	0.556-0.557	0.363 (0.002)	0.361-0.365
10^{13}	0.080 (0.001)	0.080-0.082	0.557 (0.001)	0.556-0.557	0.363 (0.001)	0.362-0.363

Table 2: Mean and standard deviation (SD), median and 2.5th ($P_{2.5}$) and 97.5th ($P_{97.5}$) percentiles of the optimal fractions for H, O and Cl for different values of the radiant intensity (Rad.Int), expressed as the number of photons per steradian [ph/sr].

References

[1] Paramonov, P. *et al.* CAD-ASTRA: a versatile and efficient mesh projector for x-ray tomography with the ASTRA-toolbox **32**, 3425 (2024). URL `https://opg.optica.org/abstract.cfm?URI=oe-32-3-3425`.

[2] Lee, S. *et al.* Additional value of dual-energy ct to differentiate between benign and malignant mediastinal tumors: An initial experience. *European Journal of Radiology* **82**, 2043–2049 (2013). URL `https://doi.org/10.1016/j.ejrad.2013.05.040`.

[3] Lee, D. *et al.* Efficient material decomposition method for dual-energy x-ray cargo inspection system **884**, 105–112. URL `https://linkinghub.elsevier.com/retrieve/pii/S0168900217313633`.

[4] Kim, G., Park, S., Lim, I., Song, K. & Kim, J.-G. Feasibility study of an improved single-energy material decomposition method for computed tomography **69**, 1366–1374 (2022). URL `https://ieeexplore.ieee.org/document/9779729/`.

[5] Alvarez, R. E. & Macovski, A. Energy-selective reconstructions in x-ray computerised tomography. *Physics in Medicine Biology* **21**, 733 (1976). URL `https://dx.doi.org/10.1088/0031-9155/21/5/002`.

[6] Kis, B. J., Sarnyai, Z., Kákonyi, R., Erdélyi, M. & Szabó, G. Single-energy material decomposition using x-ray path length estimation: **36**, 768–777 (2012). URL `http://journals.lww.com/00004728-201211000-00022`.

[7] Schaefer, J. *et al.* Simulation study of material decomposition in dual-energy radiography for bone removal. In *2022 IEEE Nuclear Science Symposium and Medical Imaging Conference (NSS/MIC)*, 1–7 (2022). URL `https://ieeexplore.ieee.org/abstract/document/10398895`.

[8] Kim, G. *et al.* Single-energy material decomposition in radiography using a three-dimensional laser scanner **75**, 153–159 (2019). URL `http://link.springer.com/10.3938/jkps.75.153`.

[9] Iuso, D., Paramonov, P., De Beenhouwer, J. & Sijbers, J. Practical multi-mesh registration for few-view poly-chromatic x-ray inspection **43**, 63 (2024). URL `https://link.springer.com/10.1007/s10921-024-01071-y`.

[10] Seltzer, S. Tables of x-ray mass attenuation coefficients and mass energy-absorption coefficients, NIST standard reference database 126 (1995). URL `http://www.nist.gov/pml/data/xraycoef/index.cfm`.

[11] NIST XCOM: Element/compound/mixture. URL `https://physics.nist.gov/PhysRefData/Xcom/html/xcom1.html`.